Available online at www.sciencedirect.com

ScienceDirect

Proceedings of the Combustion Institute 36 (2017) 3949–3958

Proceedings of the Combustion Institute

www.elsevier.com/locate/proci

Premixed methane oxycombustion in nitrogen and carbon dioxide atmospheres: measurement of operating limits, flame location and emissions. Proceedings of the Combustion Institute

R. Marsh*, J. Runyon, A. Giles, S. Morris, D. Pugh, A. Valera-Medina, P. Bowen

Cardiff University, School of Engineering, Cardiff CF24 3AA, United Kingdom

Received 3 December 2015; accepted 7 June 2016
Available online 20 June 2016

Abstract

The influence of O_2 concentration on a premixed swirling flame was investigated for changes in discrete levels of CO_2 and N_2 dilution, with application to carbon capture in gas turbine systems. Chemical kinetic models were utilised to support and analyse generic burner experiments at 37.5 kW. O_2 mole fraction in the oxygen-diluent stream was varied between 0.21 and 0.70 and careful measurement of velocity field data using particle image velocimetry, representative heat release (OH* chemiluminescence) and flame location (OH planar laser-induced fluorescence) was undertaken. Results show that under lean N_2-diluted operating conditions there is a minor change in burner operation for all O_2 concentrations considered. CO_2 dilution has a far more substantial impact than N_2 on flame location, heat release and operational response, which is attributed to the fundamental differences in thermodynamic and transport properties between the two gases. This also resulted in increased CO concentrations sampled from the exhaust stream with a rise in diluent CO_2, which is attributed to lower flame temperatures as opposed to thermal dissociation, whilst increased N_2 dilution resulted in increasing NO_X emissions.

Keywords: Swirl combustion; Oxycombustion; Carbon capture

1. Introduction

The aim of this research is to analyse the characteristics of CO_2 and N_2 diluted swirl-stabilised combustion of O_2 and CH_4 mixtures; principally to show how flame location changes in relation to O_2 mole fraction and equivalence ratio, in con-

---

* Corresponding author.
E-mail addresses: marshr@cardiff.ac.uk, marshrichard@hotmail.com (R. Marsh).

http://dx.doi.org/10.1016/j.proci.2016.06.057

Nomenclature

Da	Damköhler number
l_0	integral length scale
u'	axial velocity
α	thermal diffusivity
S_L	laminar burning velocity
ρ	density
c_P	molar heat capacity at constant pressure
λ	thermal conductivity
μ	dynamic viscosity
β	molar oxygen concentration in oxidant mixture
ϕ	equivalence ratio
S_g	geometric swirl number
Q	molar flow rate
$D_{3,2}$	Sauter mean diameter

junction with the local flow field of the swirl zone. Limited combustion research has been published in this field, where premixed or partially premixed natural gas has been burnt in O_2–CO_2 mixtures [1–10]. Recent studies on gas turbine burners used exhaust gas recirculation levels up to 30%, and research with oxygen-enhanced natural gas burners has considered molar O_2 fractions up to 40% [11,12]. Other work demonstrated stability limits of tubular burners with various O_2 and CO_2 concentrations, proving O_2–CH_4 flames can be balanced with CO_2 as a combustion moderator [13]. Studies on flame front locations demonstrated flame shape is influenced by O_2 fraction, but weakly dependent on equivalence ratio [2]. When comparing diluents, limited studies show that at constant mass flux, CO_2 diluted flames are stabilised at higher O_2 concentrations compared to N_2. Such reaction kinetics have been studied with CHEMKIN to show differences in laminar burning velocity of O_2–CH_4 mixtures with N_2 and CO_2 diluents; it should be noted also that CO_2 contributes to soot oxidization and affects the rate of many chemical reactions compared with N_2. Under stoichiometric conditions, a pure O_2–CH_4 flame exhibits flame speeds around 10 times greater than the air–CH_4 equivalent [14]. Moreover, premixed O_2–CH_4 swirl stabilised burners, also diluted with N_2 and CO_2, demonstrated dependence of strain rate through chemical kinetics and flow residence times on flame blowoff [15]. A rapidly mixed tubular burner has shown how oxygen concentration with CO_2 and N_2 diluents affected stability limits, utilising Damköhler number to describe the flow field in relation to mixing and chemical residence times [16]. This work also demonstrated that CO_2 dissociation in oxygen–methane flames is not significant at temperatures below 2400 K.

Table 1
Properties of oxygen and diluents at 1000 K and 0.1 MPa.

Substance	O_2	N_2	CO_2
ρ (kg/m^3)	0.385	0.337	0.529
c_P (J/mol.K)	34.9	32.7	54.3
λ (10^3 W/m.K)	79.7	66.0	70.6
μ (10^6 Pa.s)	49.1	41.6	41.3

1.1. Chemical timescales

Robust understanding of the phenomena governing premixed turbulent combustion involves consideration of chemical and flow timescales within the reaction zone. In the case of methane oxycombustion with variable diluents, the interaction between chemical and flow properties must be measured. These are described by consideration of the flame Damköhler number, defined in Eq. (1) as:

$$Da = \frac{(l_0/u'_{RMS})}{(\alpha/S_L^2)} = \frac{\text{flow time scale}}{\text{chemical time scale}} \tag{1}$$

Different velocity, length and chemical timescales lead to a variety of extinction conditions, thus affecting blowoff conditions [17].

Diluents affect the flame in at least four ways: (1) mixture heat capacity, (2) transport properties, (3) chemical kinetics, (4) radiative heat transfer [15]. A reduction in burning velocity is noted when N_2 is replaced by CO_2—primarily attributed to the higher heat capacity of CO_2 [18]. Table 1 shows physical properties for each substance [19].

2. Methodology

2.1. Mixture convention

Oxygen mole fraction (β) is defined as the molar ratio of oxygen in the oxygen/diluent mixture, Eq. (2), in the case of the N_2 system (where for air $\beta = 0.21$) [4]:

$$\beta = \frac{Q_{O_2}}{Q_{O_2} + Q_{N_2}} \tag{2}$$

As β is variable in the oxidant mixture, care must be taken to identify both equivalence ratio (ϕ) and β when presenting results. Since conditions studied herein were designed to evaluate the behaviour of variable O_2 content on premixed swirl burners, all data were collected in the region $\phi < 1$ and $\beta > 0.21$.

2.2. Chemical kinetics simulation

The PREMIX coded laminar flame speed calculator was utilised in CHEMKIN-PRO [20,21] to model the reactant mixtures for ambient conditions of temperature (293 K) and pressure (0.1 MPa)

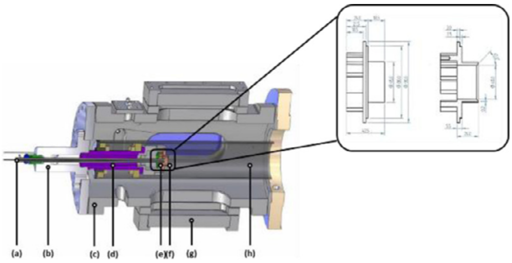

Fig. 1. Schematic diagram of the HPOC with the HPGSB installed showing (a) spark igniter, (b) inlet plenum, (c) HPOC outer casing, (d) mixing plenum, (e) radial-tangential swirler insert, (f) exit nozzle, (g) quartz window, and (h) quartz confinement. Also shown are dimensions (mm) of (e) and (f) in zoomed view.

with GRI-Mech 3.0 reaction mechanism [22]. The simulation employed 53 chemical species and 325 reactions, with solutions based on an adaptive grid of 1000 points, mixture-averaged transport properties, and trace series approximation. To examine a hypothesis relating to CO formation via thermal dissociation, the relevant mechanisms were deactivated for specific experiment points to compare this effect in CO_2 diluted combustion.

2.3. High-pressure generic swirl burner (HPGSB) testing

The high pressure optical chamber (HPOC) at Cardiff University's Gas Turbine Research Centre was used with a high-pressure generic swirl burner (HPGSB) at 37.5 kW thermal power. Premixed diluent, fuel, and oxygen entered the burner inlet plenum, travelling through a single radial-tangential swirler and out through the burner exit nozzle. Fig. 1 shows a 3-D section view of the HPGSB detail within the HPOC, including detail of the swirler and exit nozzle. The HPGSB operates with a cylindrical quartz exhaust confinement, a radial expansion ratio of 3.5 from the burner nozzle exit radius of 20 mm, and a geometric swirl number $S_g = 1.04$.

2.4. Flow field measurement via particle image velocimetry (PIV)

The particle image velocimetry (PIV) system consists of a frequency doubled (532 nm) dual cavity Nd:YAG Litron laser at 5 Hz. Laser optics (9080 × 0651) were used to transform the beam into a 1 mm thick sheet. A Hi Sense MkII Camera (C8484-52-05CP) was used, with 1.3 megapixel resolution. A 60 mm Nikon lens, fitted with a narrow bandpass filter centred at 523 nm, afforded at 90 × 120 mm field of view, with a resolution of 11.27 pixels/mm and a depth of 1.5 mm. The flow was seeded with 1.7 µm (based on $D_{3,2}$) aluminium oxide particles upstream of the burner inlet plenum. A frame-to-frame adaptive correlation technique was carried out with a minimum interrogation area of 20 × 20 to 40 × 40 pixels, with adaptability to particle density and velocity gradients. A temporally averaged velocity map was created with 189 image pairs, representing approximately 37 s at each test condition.

PIV velocity maps were utilised for identification of the flame-stabilising shear layer, identified as a line of zero axial velocity. This exists between the outward forward flow near the outside edge of the burner exit and inward flow of the central recirculation zone (CRZ). Fig. 2(a) shows the processed velocity map for a CO_2-diluted oxymethane flame at $\beta = 0.21$. The arrows represent resultant velocity vectors, providing an indication of flow direction, while vector length corresponds to resultant velocity at each location in space. The burner exit at $y = 0$ mm with the centreline located at $r = 0$ mm. The outward forward flow, shear layer, and CRZ are well-defined, with the latter indicated by areas of high reverse flow. This was transformed into a contour plot considering only the axial velocity component, with edge detection utilised to identify the shear layer, Fig. 2(b).

2.5. OH^* chemiluminescence measurements

A Dantec Hi Sense Mk II CCD camera with 1.3 megapixel resolution was coupled to a Hamamatsu C9546-03 L image intensifier for OH^* chemiluminescence measurements. A 78 mm focal length UV lens was installed on the intensifier, with a narrow band pass filter centred at 315 nm. The camera was placed viewing through the top window of the HPOC. The image plane is centred on the burner exit giving a view field of ~100 mm (radial) to 75 mm (axial) at 13.6 pix/mm. 200 images were captured at 10 Hz for each experiment, with an intensifier gate pulse of 400 μs triggered by the camera aperture. To ensure consistency between OH^* chemiluminescence measurements, the intensifier gain was held constant throughout. A modified open access Abel inversion algorithm [23] was utilised to transform the 3-D OH^* chemiluminescence image into a 2-D representation of the OH^* intensity distribution, with the underlying assumption that the swirl-stabilised flame is centreline axisymmetric [24].

2.6. Planar laser induced fluorescence (PLIF) measurements

Planar laser-induced fluorescence (PLIF) measurements were made at each experiment. The PLIF system comprised a Quantel TDL-90 dye laser pumped by the 532 nm output beam of a frequency-doubled Spectra Physics GCR 170-10 Nd:YAG laser at 10 Hz. The output beam of the TDL-90 was tuned to 283 nm to excite the (1,0) band of the OH radical, while fluorescence was

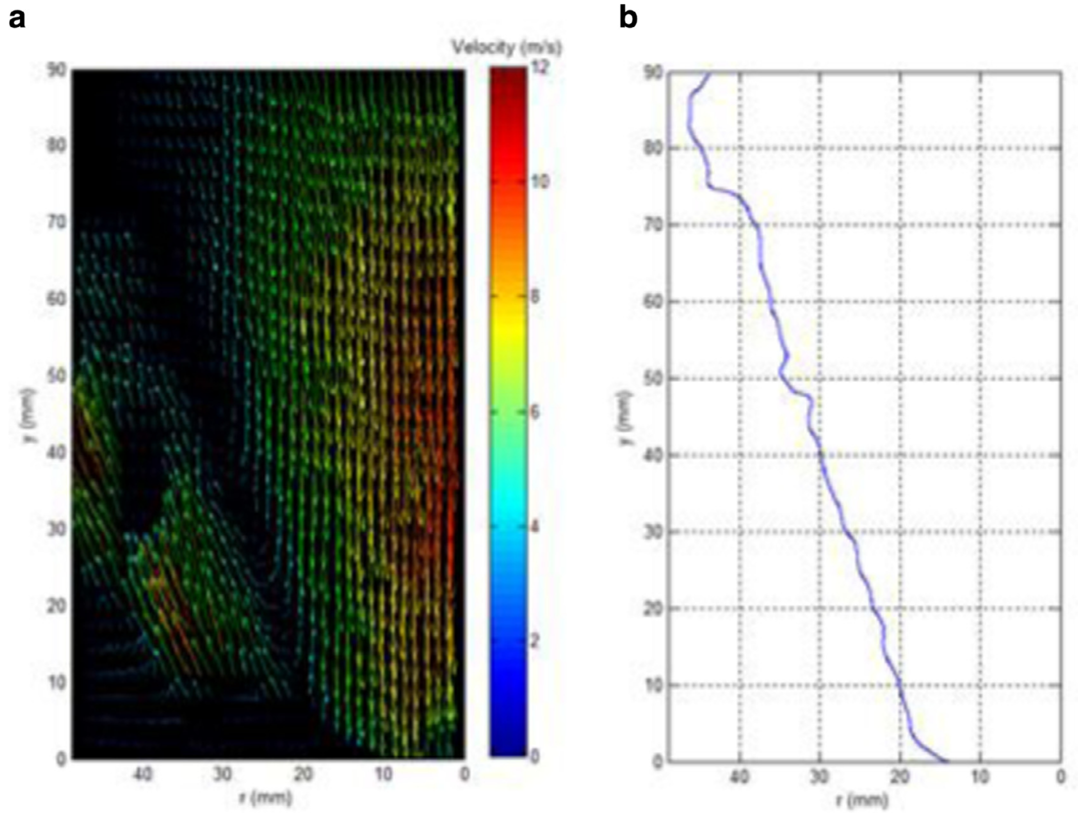

Fig. 2. PIV image processing steps with (a) fully processed PIV resultant velocity map, and (b) contour edge detection applied to show shear layer with zero axial velocity.

captured at 315 nm using the intensified CCD camera. The output beam was directed through telescopic optics providing a 25 mm wide sheet. This produced energies of ~16 mJ/pulse at 283 nm. The gate timing of the image intensifier was set to 1.5 μs and triggered by the Q-switch of the Nd:YAG laser to ensure capture of the OH PLIF signal synchronized with the laser excitation pulse. The image intensifier gain was again held constant to ensure comparability, reducing the signal-to-noise ratio. For each experiment, 500 images were taken at 10 Hz. Results were temporally averaged and corrected for background reflected light and chemiluminescence intensity. The field of view was ~100 mm (radial) by ~75 mm (axial), with resolution of 13.6 pix/mm, and the camera imaging plane shifted to focus on one half of the burner.

2.7. *Experiment conditions*

Previous research in this field examined the relationship between controlling factors of equivalence ratio and molar oxygen concentration (β) with different inert diluents, measuring flame front location and temperature [2]. Differences in physical and transport properties between N_2 and CO_2 will affect the flame in terms of heat transfer, and discrete velocities of gases in the recirculation zone, which affect mixing, flame location and heat release. Experiments were conducted at constant total molar flow rate for changes in β [4]. The experimental test points are shown in Tables 2 and 3 for N_2 and CO_2 respectively. The stable operating points of 0.654 and 0.543 mol/s (N_2 and CO_2 diluted respectively) were selected as exactly half way between the flame flashback and blowoff points at $\beta = 0.21$. It would not be possible to select a single molar flowrate that would work with both diluents due to the differences in the chemical kinetics.

3. Results

3.1. *Chemical kinetics modelling of N_2 and CO_2 diluted O_2–CH_4 flames*

Fig. 3 provides modelled laminar flame speeds and adiabatic flame temperatures (AFT) against change in equivalence ratio for each β, and specified experimental conditions. Similar trends in AFT

Table 2
Experiment conditions for N_2 diluted O_2–CH_4 flames. CH_4 flow rate is 0.047 mol/s and total flow rate is 0.654 mol/s for each condition.

Experiment	N_2 flow (mole/s)	O_2 flow (mole/s)	B	O_2:CH_4	Φ	AFT (K)
N1	0.479	0.127	0.21	2.72	0.74	1903
N2	0.419	0.188	0.30	4.01	0.50	1894
N3	0.364	0.243	0.40	5.18	0.39	1887
N4	0.303	0.303	0.50	6.47	0.31	1882
N5	0.243	0.364	0.60	7.77	0.26	1873
N6	0.182	0.425	0.70	9.06	0.22	1867

Table 3
Experiment conditions for CO_2 diluted O_2–CH_4 flames. CH_4 flow rate is 0.047 mol/s and total flow rate is 0.543 mol/s for each condition.

Experiment	CO_2 flow (mole/s)	O_2 flow (mole/s)	B	O_2:CH_4	Φ	AFT (K)
C1	0.390	0.104	0.21	2.21	0.90	1683
C2	0.341	0.153	0.30	3.27	0.61	1723
C3	0.296	0.198	0.40	4.22	0.47	1763
C4	0.247	0.247	0.50	5.27	0.38	1809
C5	0.198	0.296	0.60	6.32	0.32	1859
C6	0.148	0.346	0.70	7.38	0.27	1912

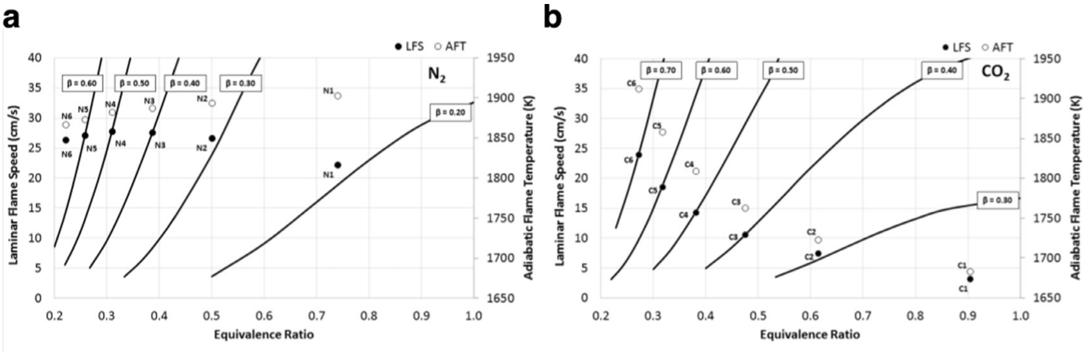

Fig. 3. Effect of β shown as predicted laminar flame speed (LFS) and AFT versus $\O$ for O_2–CH_4 flames diluted with (a) N_2 and (b) CO_2, with experiment points highlighted. Solid lines representing LFS at constant β is also shown.

and flame speed are evident for both diluents, with CO_2 shown to provide greater change in flame temperature for increasing β; rising with O_2 fraction, compared to the smaller opposing influence simulated for N_2. The results are in agreement with the simulation work of Liu et al. [14].

3.2. *Confined HPGSB experiments at 37.5 kW with flow and flame analysis*

Direct comparison could not be made with identical flow rates for both diluents, given that the N_2 and CO_2 diluted flames had different flame stability envelopes. All results in the N_2-diluted system were taken at a total premixed molar flow rate of 0.654 moles/s and CO_2-diluted measurements at 0.543 moles/s. Since these experiments were undertaken at constant molar flow rates, flame and flowfield changes result from changes in:

- Gas density, therefore recirculation zones.
- AFT.
- Kinetic interaction between reactive and passive species [15].
- Radiative absorption and emission.

Referring to Fig. 3, the initial observations regarding CO_2 tendency for blowoff become clear since there is a greater difference in flame speed and temperature over ranges tested for the CO_2-diluted system. The influence of the two diluents on overall heat release is shown in Fig. 4 using Abel inverted OH* chemiluminescence, indicating the conical flame shape expected in a swirl-stabilised burner such as this. This shows the influence of O_2 fraction on the two diluted flames with constant molar flow rate. There is clear difference between these indicative heat release results at different β values, which correlates with CHEMKIN simulations in Fig. 3. Starting at $\beta = 0.21$ (air) for the

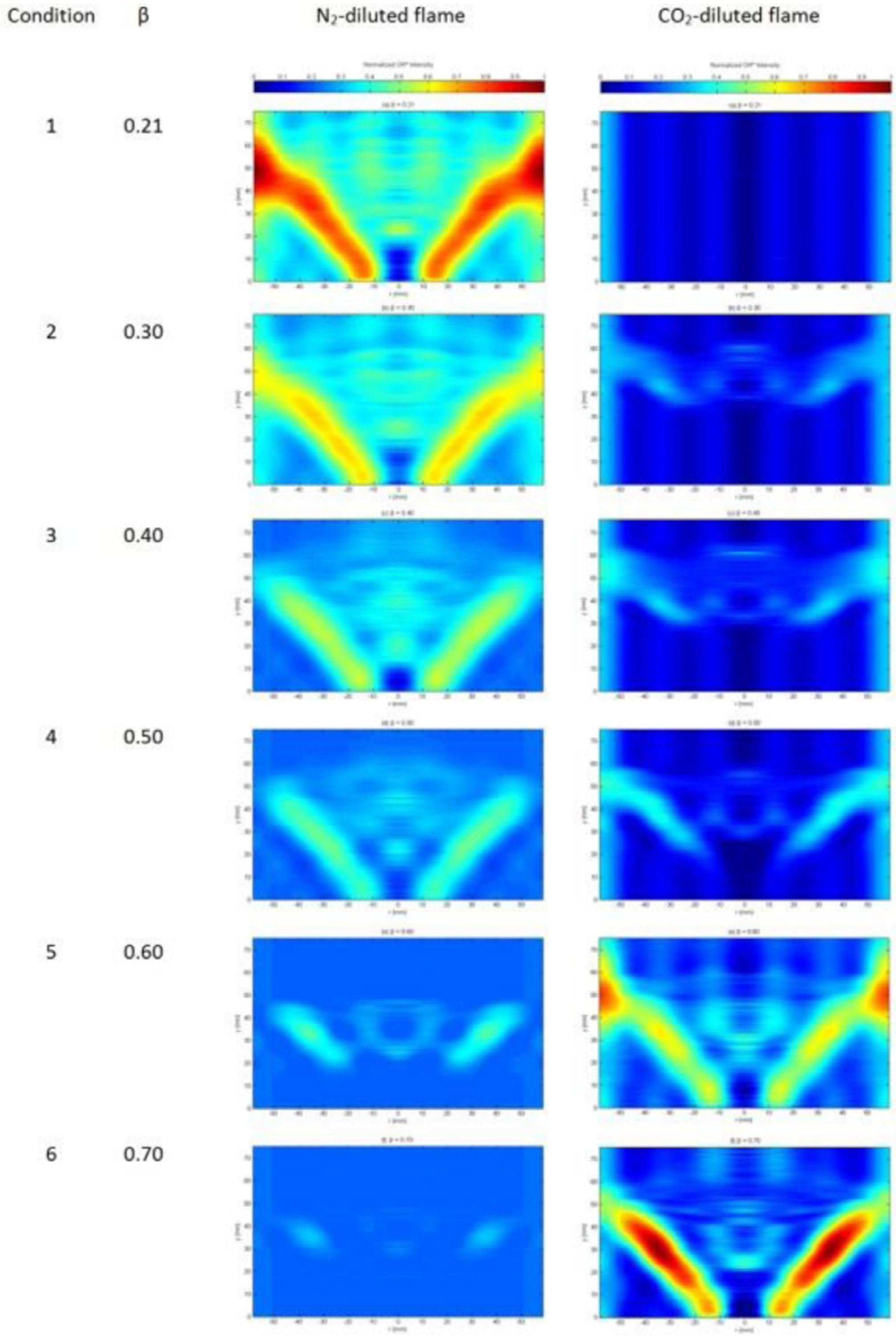

Fig. 4. Abel deconvoluted and normalized OH*chemiluminescence images for N_2-diluted (left) and CO_2-diluted (right) with increasing O_2 concentration in the premixed reactants ($\beta = 0.21$ to $\beta = 0.70$).

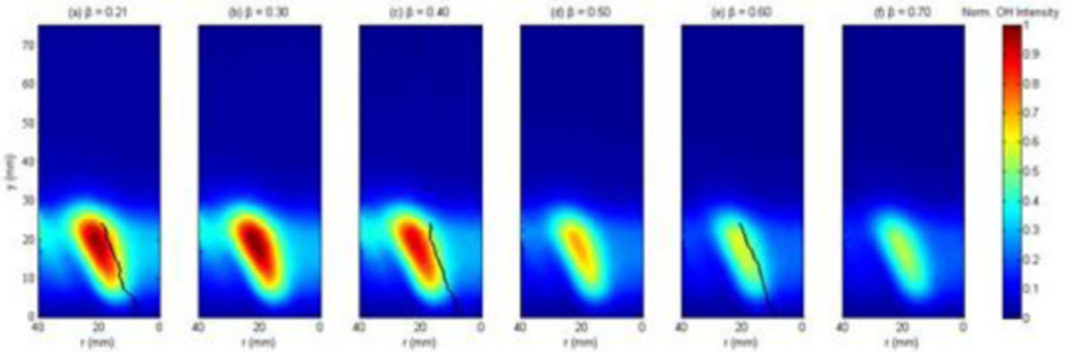

Fig. 5. Normalised OH PLIF results for the N_2-diluted flame with condition (a) N1 ($\beta = 0.21$) to (f) N6 ($\beta = 0.70$). Axial shear boundary lines from PIV are included in (a), (c), and (e).

N_2-diluted case, increasing the O_2 concentration reduces the OH* emission intensity across the flame. The flame appears more lifted with increasing β (most notably at $\beta = 0.60$) resulting from the reduction in AFT, and overall reaction rate as O_2 fraction increases.

For the case of CO_2 dilution, the flame at $\beta = 0.21$ was detached from the burner, close to the blowoff point, thus out of the field of view. The increase in O_2 concentration had a significant effect on flame position, causing OH* emission to increase, allowing the flame to attach in the shear zone, correlating with changes presented for increasing β in Fig. 3. At $\beta = 0.70$, the CO_2-diluted flame was comparable to a low β N_2-diluted flame, given the similarity in flame speed, temperature and transport properties, as the mixture was comprised largely of O_2 with comparable transport properties to N_2.

Comparing diluent properties for these mixtures, the resultant kinetics of CO_2-diluted combustion gives rise to significantly cooler, slower flames. Molar heat capacity and density increase with CO_2 whereas they decrease with N_2; the reverse is true for thermal conductivity. This results in the observed downstream migration of the reaction zone as chemical timescales are increased. Since volumetric and flow timescales are nominally identical for each set of diluents (as confirmed by PIV) it can be said that flame migration is predominantly due to changes in chemical timescales only.

Fig. 5 shows OH PLIF data for the N_2-diluted flame operating from $\beta = 0.21$ to 0.70. OH PLIF intensity was normalised with respect to the highest measured value across the range. Images show half the flame in axial view, hence the $r = 0$ mm line represents the burner centreline. Also included in the image for $\beta = 0.21$, 0.40 and 0.60 are PIV measured axial shear lines. The flame front doesn't appear to shift significantly over the conditions, although OH intensity near the burner exit does appear to weaken as β increases and flame temperatures are reduced. This corresponds to OH* chemiluminescence (Fig. 4) which showed areas of significant heat release moving further downstream from the burner exit whilst diminishing in overall size. When the PIV data is superimposed in Fig. 5(a), (c) and (e), it is observed that the flame front is located on the outer edge of the axial shear layer, enclosing the inner recirculation zone. As β increases, the interaction between the flame front and the shear zone doesn't appear to change. Hence despite the small reduction in flame speed and temperature, the flowfield wasn't significantly affected.

Fig. 6 shows the OH PLIF data for the CO_2-diluted flame operating from $\beta = 0.21$ to 0.70. It is clear that β has a greater effect on the flame front location in the CO_2-diluted case compared to N_2 dilution. The PLIF laser setup is such that a 25 mm wide laser sheet is introduced into the burner through a side window. Thus, the horizontal excitation plane is positioned at the burner exit and covers a distance 25 mm downstream, equal to the width of the laser sheet. Included in the image for $\beta = 0.21$, 0.40 and 0.60 are the measured axial shear lines. The images show that for highest values of $\beta = 0.60$ and 0.70, where the flame speed of the mixture is highest, flame location is similarly located to that of the N_2-diluted flame (stabilised on the outer edge of the axial shear layer enclosing the inner shear zone at the burner exit). In this CO_2-diluted case, when β is decreased the flame speed decreases sharply (Fig. 3) causing the flame front to move downstream and ultimately into the recirculation zone itself. This is visible in the $\beta = 0.21$ image in Fig. 6(a), where the flame has migrated out of the swirling shear layer and stabilised inside the CRZ. Coupled with the fact that the CO_2-diluted flame visually appeared to be in a near blow-off condition at $\beta = 0.21$, OH radicals in Fig. 6(f) are the result of significant change in mixture reactivity at high CO_2

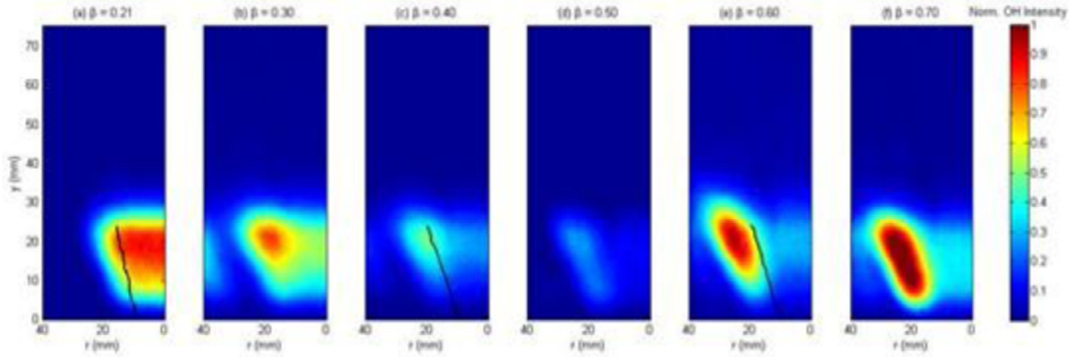

Fig. 6. Normalised OH PLIF results for the CO_2-diluted flame, with condition (a) C1 ($\beta = 0.21$) to (f) C6 ($\beta = 0.70$). Axial shear boundary lines from PIV are included in (a), (c), and (e).

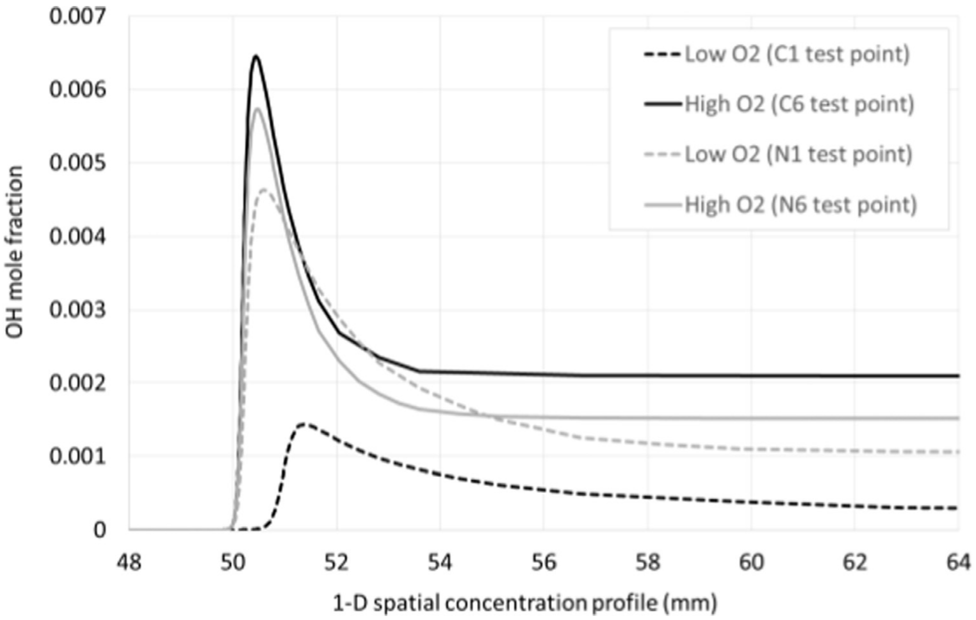

Fig. 7. CHEMKIN results showing OH 1-D spatial concentration profiles for given conditions.

dilution. Under these conditions, flame speed and AFT reduce significantly, the flame moves further downstream and the retarded reactions then occur within the CRZ, as OH radicals are recirculated towards the burner exit. For $\beta = 0.70$, the amount of CO_2 is relatively low, increasing the flame temperature, and thus yielding a flame shape and location similar to that of a N_2-diluted flame at $\beta = 0.21$. From $\beta = 0.40$ (Fig. 6(c)) to $\beta = 0.21$ (Fig. 6(a)), the increasing OH PLIF intensity indicates a transition in flame stabilisation location, as the OH PLIF intensity increases in the CRZ, marking significant changes from shear layer stabilisation at $\beta = 0.70$. In Fig. 6(d), at $\beta = 0.50$, the flame is still stabilised in the shear layer but the flame front has moved out of excitation plane of the PLIF laser.

Referring to Eq. (1), where the relationship between chemical timescales and hydrodynamic behaviour was introduced, it can be seen that the flowfield shape has remained largely unaffected by the heat release location (Fig. 4) for both diluents. Hence although there is a difference in transport properties between N_2 and CO_2, this doesn't appear to significantly alter the turbulence structure in the flame zone. As a result of this it can be expected that the *Da* through the N_2 diluted cases has changed relatively little, whereas the change through the CO_2 cases is significant.

Fig. 7 provides example 1-D OH spatial concentration profiles generated for the extreme N_2 and CO_2 diluted cases (N1, N6, C1, and C6) using the PREMIX solver. This suggests an increase in OH

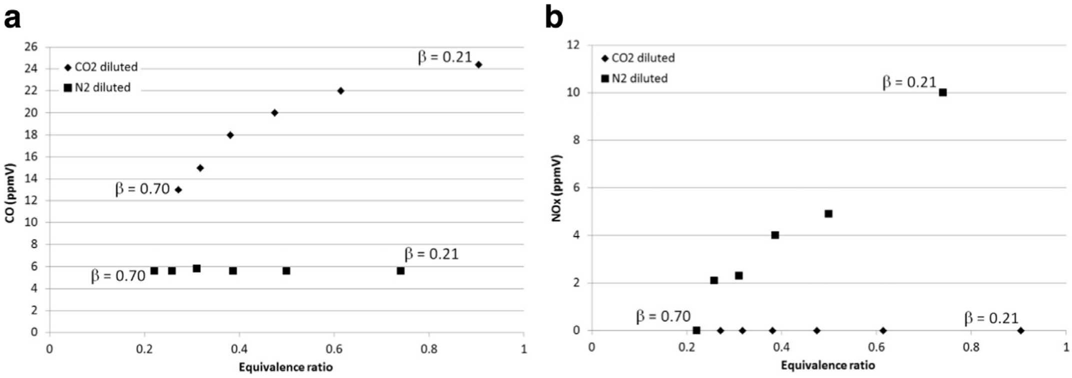

Fig. 8. Measured exhaust gas concentrations of CO and NO_X for the two diluents at varying β values.

fraction, as would be expected, with increased levels of O_2. Note that OH fractions in the N1 and N6 case are similar which correlates with the OH PLIF results (Fig. 5). The OH profile in the C6 case is closer to all N_2 diluted cases in addition to having similar AFT and flame speed (Fig. 3), again demonstrating a similar correlation with the PLIF results (Figs. 5 and 6). This suggests the change in overall reaction rate and AFT is significantly more influential for flame stabilisation when compared to transport, and hence diffusive properties.

3.3. Exhaust gas concentrations (CO and NO_X)

The exhaust stream was sampled using a water-conditioned averaging probe (9 holes) located approximately 10 diameters downstream of the combustor exit. The probe and sample line were maintained at 433 K, with a heated pump used to deliver products to the analysis suite. Hot NO_x concentrations were quantified using a heated vacuum chemiluminescence analyser (Signal Instruments 4000VM), calibrated in the range 0–39 ppmV. A chiller was also employed to reduce the molar water concentration below 1%, with downstream CO concentrations measured using a nondispersive infrared analyser (Signal instruments 9000MGA), calibrated in the range 0–904 ppmV. Fig. 8 shows the resultant CO and NO_X concentrations. Data have not been normalised to account for effective dilution in the product stream, because equivalent volumetric flow rates are maintained for all tests. Raw CO concentrations are presented cold/dry, and NO_x, hot/wet. This was to remove the uncertainty associated with normalising data to an assumed water concentration in the product stream, therefore only qualitative trends in the plots are considered.

Results demonstrate an expected absence of NO_X chemistry in the CO_2 diluted flame, plus the unaffected emission of CO across the range of $\beta = 0.21$–0.70 exhibited by the N_2-diluted flame. This was to be expected considering the small different in AFT, and limited weakening of the flame with the N_2 experiments. NO_x production rises with an increase in initial N_2, and hotter temperatures. There is an increase in CO production as CO_2 concentrations rise to $\beta = 0.21$ in the CO_2-diluted flame, whilst a corresponding change in N_2 leads to increased NO_X formation. Whilst it could be suggested that CO emissions are a product of CO_2 thermal dissociation, it is more likely that the CO is a product of incomplete methane combustion owing to the reduced AFT and increased reaction times of the mixture. Further CHEMKIN simulations were undertaken to determine whether CO_2 diluent could have an effect on CO production via thermal dissociation. This showed the difference between the base mechanism (normal GRI-MECH) and the mechanism without thermal dissociation is barely noticeable. The results agree with historical work [25] undertaken at various temperatures ranging from 1300 to 3320 °C, showing that below 1500 °C CO_2 dissociation to CO was extremely low compared to cases above 2000 °C. Since average temperatures of the flame are below this peak value, it was recognized that CO was mostly present as a consequence of incomplete combustion.

4. Conclusions

- At constant volumetric flow rate in a stable premixed swirl flame, changing β in N_2-diluted flames has marginal effect on burning velocity and hence flame location, heat release and CRZ shape.
- Where CO_2 is the diluent, the effect of changing β is significant and measureable under the conditions considered. Flame temperature decreases, and reaction kinetics are sufficiently slowed that the flame zone moves downstream and eventually stabilises in the CRZ.

- PIV results show minimal difference between the location of the shear layer in the $\beta = 0.21$, 0.40 and 0.60 flowfields for N_2 and CO_2 diluted combustion, hence the structure is largely unaffected, even with the OH* chemiluminescence and OH PLIF data showing a measurable difference in flame zone location.
- Higher concentrations of CO_2 led to increases in CO in the exhaust, attributed to lower flame temperatures as opposed to dissociation, whilst an increase in NO_x production was observed with an increase in N_2 concentration.

Acknowledgments

This work was funded via the UK's Engineering and Physical Sciences Research Council, under the SELECT project, EP/M001482/1.

References

[1] J. Runyon, R. Marsh, A. Valera-Medina, A. Giles, P. Bowen, GT2015-43588, *ASME Turbo Expo Montreal* (2015), p. V04BT04A043 (13 pages).
[2] P. Kutne, B. Kapadia, W. Meier, M. Aigner, *Proc. Combust. Inst.* 33 (2011) 3383–3390.
[3] P. Rokke, J. Hustad, *Int. J. Thermodyn.* 8 (4) (2005) 167–173.
[4] B. Shi, J. Hou, S. Ishizuka, *Combust. Flame* 161 (5) (2014) 1310–1325.
[5] M. Habib, M. Nemitallah, P. Ahmed, M. Sharqawy, H. Badr, I. Muhammad, M. Yaqub, *Energy* 86 (2015) 105–114.
[6] P. Heil, D. Toporov, M. Forster, R. Kneer, *Proc. Combust. Inst.* 33 (2011) 3407–3413.
[7] G. Krieger, A. Campos, M. Takehara, F. Alfaia da Cunha, C. Gurgel Veras, *Appl. Therm. Eng.* 78 (2015) 471–481.
[8] C. Liu, G. Chen, N. Sipöcz, M. Assadi, X. Bai, *Appl. Energy* 89 (2012) 387–394.
[9] A.P. Shroll, S.J. Shanbhogue, A.F. Ghoniem, *J. Eng. Gas Turbine Power* 134 (2012) 051504–051501.
[10] S. Sundkvist, A. Dahlquist, J. Janczewski, M. Sjodin, M. Bysveen, M. Ditaranto, Ø. Langørgen, M. Seljeskog, M. Siljan, *J. Eng. Gas. Turb. Power* 136 (2014) 101513–101511.
[11] A. Evulet, A. Elkady, A. Brand, D. Chinn, *Energy Proc.* 1 (2009) 3809–3816.
[12] R. Anderson, S. McAdam, F. Vitelli, O. Davies, J. Downs, A. Paliszewski, GT2008-G51377, *ASME Turbo Expo Berlin* (2008), p. 781–791.
[13] B. Dam, N. Love, A. Choudhuri, *Energy Fuels* 27 1 (2013) 523–529.
[14] F. Liu, H. Guo, G. Smallwood, *Combust. Flame* 133 4 (2003) 495–497.
[15] A. Amato, B. Hudak, P. D'Carlo, D. Noble, D. Scarborough, J. Seitzman, T. Lieuwen, *J. Eng. Gas Turb. Power* 133 (6) (2011) 061503 (9 pages).
[16] B. Shi, J. Hou, S. Ishizuka, *Combust. Flame* 162 (2) (2015) 420–430.
[17] G. Ballachey, M. Johnson, *Proc. Combust. Inst.* 34 (2013) 3193–3201.
[18] J. Bibrzycki, T. T. Poinsot, in: Working note EC-COMET WN/CFD/10/17, 2010.
[19] NIST chemistry web-book. http://webbook.nist.gov/chemistry/; 2015; Accessed 01/12/2015.
[20] Reaction Design, CHEMKIN-PRO 15092, Reaction Design: San Diego, (2009).
[21] Reaction Design, CHEMKIN-PRO Theory Manual, PRO-THE-15092-UG-1, San Diego, (2009).
[22] http://www.me.berkeley.edu/gri-mech/; 2015 Accessed 01/12/2015.
[23] http://www.mathworks.com/matlabcentral/fileexchange/43639-abel-inversion-algorithm; 2015 Accessed 01/12/2015.
[24] J. Runyon, R. Marsh, Y. Sevcenco, D. Pugh, S. Morris, in: Proc. 7th Europ. Combust. Meet., 2015, pp. 3–29.
[25] R. Fenning, H. Tizard, *Proc. Royal Society A* 115 (1927) 318–333.